PHYSICAL REVIEW B **88**, 155316 (2013)

Magnetic-field-dependent spin decoherence and dephasing in room-temperature CdSe nanocrystal quantum dots

A. Khastehdel Fumani and J. Berezovsky*
Department of Physics, Case Western Reserve University, Cleveland, Ohio 44106, USA
(Received 23 August 2013; published 21 October 2013)

We perform and analyze a series of time-resolved Faraday rotation measurements of coherent spin dynamics in a room-temperature ensemble of CdSe nanocrystal quantum dots (NCQDs) to study the decoherence and dephasing mechanisms that limit the transverse spin lifetime. Coherent spin lifetimes on the order of nanoseconds have been previously observed in CdSe NCQDs, but the presence of multiple components with distinct dynamics and strong inhomogeneous dephasing have made it difficult to study the relevant spin decay mechanisms quantitatively. Here, we obtain reliable fitting results by ensuring that cross-correlations between model parameters are minimized for the parameters of interest. Furthermore, we characterize the morphological inhomogeneity of the NCQD ensemble using transmission electron microscopy to constrain the model parameters that specify inhomogeneous dephasing. We find that g-factor inhomogeneity-induced dephasing (gID) is not sufficient to explain the magnetic-field-dependent decay of the spin signal. We propose an additional decoherence mechanism arising from rapid transitions between the fine structure states of the exciton referred to as fine-structure decoherence (FSD). By including both gID and FSD in the model, excellent fits are obtained to the data, including a prominent short-time-scale feature, which has typically been excluded from the fits in previous work.

DOI: 10.1103/PhysRevB.88.155316 PACS number(s): 78.67.Hc, 71.35.Ji, 78.47.da, 78.66.Hf

I. INTRODUCTION

Control of spin coherence in semiconductors opens the route to new technologies ranging from spintronics to quantum information processing.[1,2] If such control can be achieved at room temperature in conventional semiconducting materials, the possibility for practical devices is greatly increased. Semiconductor nanocrystal quantum dots (NCQDs) are a promising platform for studying, controlling, and exploiting room-temperature spin coherence.[3,4] Previous work has observed spin coherence lifetime $\tau \approx 2$ ns in NCQDs synthesized from II-VI semiconductors (e.g., CdSe), at room temperature.[5,6] In order to exploit spins in these materials, it will be necessary to understand and control the mechanisms that limit the spin coherence.[7,8]

There are primarily two confounding factors that arise in studying the spin decay mechanisms in NCQDs. First, measurements of spin dynamics in NCQD ensembles generally show the sum of two distinct components, referred to here as S_1 and S_2 components, with different dynamics and decay characteristics. Second, in these ensemble measurements, inhomogeneous dephasing plays a significant role in the decay of the spin signal, particularly, in transverse magnetic field $B \neq 0$. These effects must be disentangled in order to accurately measure dephasing and decoherence processes.

In this work, we investigate the spin decoherence and dephasing behavior present in an NCQD ensemble by fitting time-resolved Faraday rotation data to predicted models in different applied magnetic fields. We focus on the low magnetic field regime where the strength of both decoherence and dephasing processes are comparable. Given the presence of two distinct components both exhibiting dephasing and decoherence processes, the predicted models will necessarily have significant numbers of parameters. In order to achieve reliable fitting results, it is critical to constrain as many parameters as possible, and examine cross-correlations between free parameters. We image individual NCQDs from the same ensemble using transmission electron microscopy (TEM). This permits quantitative characterization of the morphological inhomogeneity of the NCQD ensemble, thereby constraining some of the parameters in the model. We then optimize the form of the model function to minimize cross-correlation between parameters, and to isolate correlations in parameters that are not of interest.

We find that the data are not well described by a model of B-independent decoherence, and B-dependent inhomogeneous dephasing, as has previously been suggested.[9] We describe an additional decoherence mechanism, referred to as fine-structure decoherence (FSD), arising from fluctuations among the electron-hole exchange- and crystal field-split fine-structure levels of the exciton ground state. By including FSD in the model function, the data are well fit at all magnetic fields, including a prominent short-time-scale feature, which had necessitated *ad hoc* treatment in previous models. The FSD mechanism also provides a resolution to the open question of how long-lived carrier spin coherence coexists with the much shorter lifetime of the exciton spin state itself.[10]

The fitting procedure used here allows us to extract reliable values for the spin lifetimes at $B = 0$, with associated uncertainties. We find zero-field lifetimes for the S_1 and S_2 components of several nanoseconds, but with significantly different values. This indicates that the two components arise from distinct subensembles of NCQDs subject to different decoherence and dephasing processes. In Conclusion, we will discuss the possible mechanisms that may be ultimately limiting these spin lifetimes.

The paper is organized in the following way. In Sec. II, we review the electronic structure, optical spin pumping, spin dynamics, and optical spin detection in NCQDs. Then we present a general model for the measured FR signal. In Sec. III, the FR measurement setup and the method used to find the size and shape distribution within the NCQD ensemble is described. In Sec. IV, we present the FR data, and first compare to the gID model. Next, we describe the FSD mechanism and

 ©2013 American Physical Society

compare the data to a model including both gID and FSD. In Sec. V, we discuss the results in the context of previous works and present conclusions.

II. THEORY AND BACKGROUND

A. Electronic structure of NCQDs

In CdSe NCQDs with a radius of several nanometers, quantum confinement splits the valence and conduction band electronic states by tens or hundreds of meV, providing confined quantum dot behavior at room temperature. The energy level spectrum may be calculated from effective mass theory,[11] assuming a spherical confining potential. Imposing different boundary conditions models the contribution of surface structure to the quantum size levels and to the electron magnetic moment in NCQDs.[12] The lowest-energy conduction band level, designated $1S_e$ is separated from the next lowest-energy level by several hundred meV, while the highest-energy valence band state (lowest-energy hole state), designated $1S_{3/2}$, is separated from the next hole level by several tens of meV. Therefore the energy difference between electron levels is much larger than thermal energy at room temperature, and the energy difference between hole levels is on the same order as the thermal energy.

The spectrum of electron-hole (exciton) states in NCQDs displays significant fine structure splitting (FSS) in addition to the size levels due to confinement.[13] In the absence of FSS, the electron with spin $S = 1/2$ and hole with angular momentum $J = 3/2$ give rise to an eightfold degenerate exciton level. Given the strong quantum confinement in NCQDs the electron-hole exchange interaction yields splittings on the order of tens of meV. When deviations from spherical symmetry are included due to an ellipsoidal NCQD shape and the wurtzite crystal structure, one finds that the excitonic levels are further split, with contributions from these effects also on the order of 10 meV. The result of the FSS is that in the lowest-energy exciton size level the degeneracy is generally lifted into five energy levels. Figure 1(a) illustrates the ground state of a neutral quantum dot (no exciton), and the first exciton state ($1S_e1S_{3/2}$) split into five levels, labeled by their angular momentum projection F along the crystal c axis. The five levels are made up of three Kramers doublets, one with $F = \pm 2$ and two with $F = \pm 1$, and two levels with $F = 0$, where the superscripts "L" and "U" denote symmetric and antisymmetric superpositions of basis states.

Figure 1(b) shows the FSS of the $1S_e1S_{3/2}$ exciton calculated using the method of Ref. 14. The NCQDs are taken to be ellipsoidal with an ellipticity $\mu = a/b - 1$, where a and b are the semimajor and semiminor axes, respectively. Figure 1(b) shows the FSS versus mean diameter d of the QDs with a fixed ellipticity $\mu = 0.41$, and Fig. 1(c) shows the FSS versus μ with fixed $d = 6$ nm. The FSS depends strongly on both NCQD size and shape, and will play an important role in our understanding of spin dynamics in NCQD ensembles. As is apparent in Figs. 1(b) and 1(c), there is a particular value $\mu_{qs}(d)$ of the ellipticity where in an NCQD with mean diameter d the crystal field and shape anisotropy contributions to the FSS cancel each other for the sets of symmetric and antisymmetric states. An NCQD with this combination of

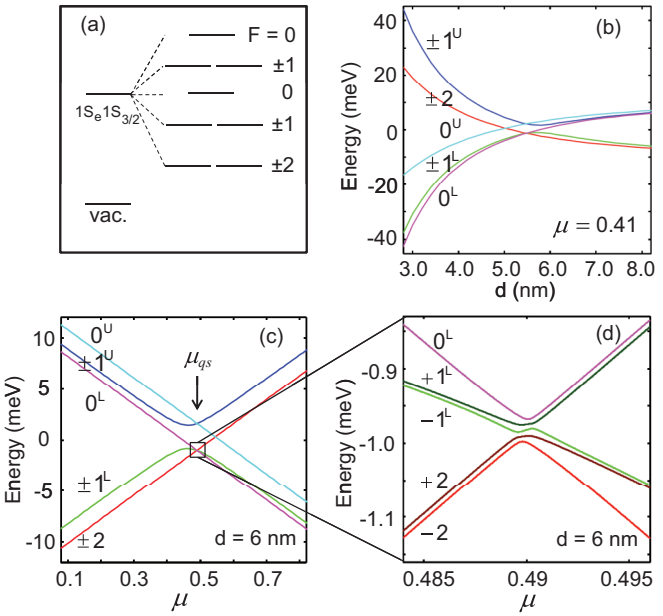

FIG. 1. (Color online) (a) Ground state of a neutral quantum dot and five exciton states labeled by their angular momentum projection along the crystal c axis. (b) FSS of a prolate CdSe QD with $\mu = 0.41$. (c) FSS of an NCQD with $d = 6$ nm vs ellipticity. (d) FSS of a $d = 6$ nm NCQD vs ellipticity near the quasispherical point in presence of a 0.1 T magnetic field.

size and shape is referred to as "quasispherical" because the effects that define a unique NCQD axis are canceled, leaving the spherically symmetric electron-hole exchange interaction as the only source of intrinsic FSS.[14] A lone hole in the NCQD also displays strong FSS, which cancels out at μ_{qs}. The subpopulation of NCQDs at or near μ_{qs} has been proposed to play an important role in the observed long-lived spin dynamics.[9] We will see below that a model that includes this effect can well-reproduce our data.

An applied magnetic field lifts the degeneracy of the three Kramers doublets, resulting in exciton FSS with eight nondegenerate levels. Away from μ_{qs} where the spacing between the Kramers doublets is large compared with the Zeeman energy, the Zeeman splitting can be treated perturbatively. Near μ_{qs}, however, the addition of a magnetic field mixes the exciton eigenstates yielding two anticrossings of the energy levels. Figure 1(d) shows the anticrossing with lower energy.

B. Spins in NCQDs

1. Optical spin pumping

Optical spin pumping is achieved when the selection rules allow preferential excitation of electrons and/or holes with a particular spin projection. A circularly polarized photon propagating parallel to the crystal c axis can create an $F = \pm 1$ exciton depending on the photon helicity, whereas propagation perpendicular to the c axis can excite only into the $F = 0$ exciton state.[15] In the ensemble of randomly oriented NCQDs studied here, the circularly polarized photons generate a net spin polarization, a superposition of $F = \pm 1$, in the suitably oriented NCQDs. In this work, the pump generates excitons in higher quantum size levels, and we assume that these

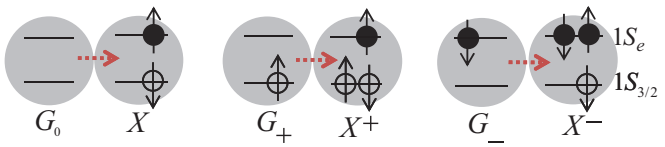

FIG. 2. (Color online) Charge states of NCQDs. Three possible ground-state charge configurations, G_0, G_+, and G_- along with the three resultant excitonic states upon optical excitation, X, X^+, and X^-.

states rapidly (<1 ps) decay to the lowest exciton level[16] with minimal change in the spin state. This assumption is supported by the similarity of the spin dynamics presented here to those resulting from resonant pumping in the same sample (not shown).

The result of optical pumping depends on the initial state of the NCQD. As has been widely studied, intermittency of the fluorescence from individual NCQDs (blinking) reveals the existence of several possible metastable ground states.[17] These are usually attributed to different charge states of the NCQD. Here, we will consider possible optical excitation from three ground states, G_+ consisting of a single hole in the valence band, G_- consisting of a single electron in the conduction band, and G_0 consisting of no holes or electrons. Here, the energy of the optical excitation is resonant with higher-energy transitions, so we do not need to consider Pauli blocking during the spin pumping process. After the optical excitation and subsequent rapid energy relaxation, the final state depends on the initial ground state as shown in Fig. 2. The G_- ground state results in a two electrons and a hole (negative trion, X^-), the G_+ ground state results in two holes and an electron (positive trion X^+), and the G_0 ground state results in a neutral exciton X. Excitation into the X state results in one of the exciton states shown in Fig. 1(a) (or a linear combination thereof). For excitation into the X^+ state, we can assume that the holes rapidly relax into a spin-zero state, leaving the twofold degenerate electron spin as the only spin. Likewise, the X^- state results in a pair of electrons in a spin zero state with the lone hole comprising the only spin.

2. Spin dynamics

Once an $F = \pm 1$ exciton has been optically pumped, it may make transitions to other exciton states with finite probabilities. Transient grating spectroscopy has provided a tool to measure these transition probabilities in NCQDs.[18] In general, the exciton states have lifetimes on the order of picoseconds. These transitions may take place by an electron or hole spin flip with inverse rates $\tau_e \sim 1$ ns and $\tau_h \sim 1$ ps, respectively.[10,19,20] Transitions between exciton states involving a change in both the electron and hole states are also possible, but will be neglected here for simplicity. Though the exciton state is changed on the time scale of τ_h, the electron spin state may persist for a longer time. The measurements presented here are sensitive to both the electron and hole spins regardless of the particular exciton state.

When the spin of an NCQD is in a superposition of eigenstates, the state evolves in time with a relative phase accumulating to each eigenstate at a rate proportional to the energy of that eigenstate. In the simplest case of a lone electron in a transverse magnetic field B, this results in coherent spin precession at a frequency $\omega = \Delta E_Z/\hbar = g\mu_B B/\hbar$, where ΔE_Z is the Zeeman energy, μ_B is the Bohr magneton, $\hbar$ is Planck's constant, and g is the effective g factor in the NCQD. For typical magnetic fields $B \sim 1$ T, this results in $\omega \sim 100$ GHz. Compared to the g factor in bulk CdSe, quantum confinement in the NCQDs shifts the electron g factor[9,12]

$$g_e(E) = g_0 - \frac{2}{3}\frac{E_p \Delta_{\mathrm{so}}}{(E_g + E + \Delta_{\mathrm{so}})(E_g + E)}, \qquad (1)$$

where g_0 is the free electron g factor, E_p is the Kane energy parameter, Δ_{so} is the spin-orbit splitting of the valence band, E_g is the semiconductor band gap, and the size dependence is introduced via electron energy E. In the general case of an exciton in a superposition of fine-structure-split NCQD states, the large energy splitting between eigenstates (∼1 meV), gives rise to very rapid evolution of the state ($\omega \sim 1$ THz). The exception to this fast dynamics occurs near μ_{qs} where an exciton state composed of a superposition of eigenstates from the upper or lower manifold of fine-structure states has splitting on the order of ΔE_Z as shown in Fig. 1(d). For an exciton in a quasispherical NCQD, Gupta *et al.*[9] find the g factor $g_{\mathrm{exc}} = (g_e - 3g_h)/2$, where the size dependence arises from g_e, and g_h is taken to be constant. In that work, Eq. (1) is found to predict the size dependence of the g factor of the S_1 component, whereas g_{exc} is found to match the S_2 g factor with reasonable accuracy. This leads to the assignment of the S_1 component to lone electron spins, either in the X^+ state or after recombination of the X^- state, and assignment of the S_2 component to spins in the X state. This assignment is confirmed by the quenching of the S_2 component upon electrochemical charging of NCQDs.[21]

An exciton initially in a coherent state will be randomized after some finite time due to decoherence processes. Furthermore, slowly varying effective magnetic fields (e.g., from the hyperfine interaction with nuclear spins) may cause dephasing in a time averaged measurement.[22,23] Since the measurements presented here do not distinguish the time scales associated with these decoherence and dephasing processes, we will combine them into a single decay time τ, with the decay described by an exponential function $\exp(-t/\tau)$. Magnetic-field-dependent ensemble averaging effects, such as dephasing due to the inhomogeneity of g factors or inhomogeneity of decoherence times, are not included in τ, and will be discussed separately.

3. Spin detection

In this work, the Faraday effect is used to measure a projection of the spin state in the ensemble of NCQDs. The Faraday effect arises from a difference in the index of refraction Δn for right and left circularly polarized light induced by spin polarization. In this case, Δn primarily arises from Pauli blocking of optical transitions with selection rules involving circularly polarized light. In these experiments, Δn is measured as a polarization rotation of linearly polarized light.[24,25]

Faraday effect measurements are sensitive to both electron and/or hole spin. If an $F = +1$ exciton is generated by σ^+

excitation and then the hole spin is rapidly flipped, the electron spin still blocks that transition or other transitions involving the same electron state for σ^+ photons. This aspect of Faraday-effect based measurements explains why a spin signal can still be measured well beyond the spin lifetime of the exciton state.

C. Model for spin dynamics in NCQDs

In this section, we will develop a general model for the Faraday rotation signal from the ensemble of NCQDs observed in these experiments. Beginning with the simple case of a single NCQD in a transverse magnetic field, a spin-polarized exciton is generated at time $t = 0$ into a superposition of eigenstates and then precesses at frequency $\omega = g\mu_B B/\hbar$. The state is randomized with a characteristic time τ, and so repeated initialization and measurement yield an exponential decay of the signal. Measuring a projection of this spin state versus t yields Faraday rotation signal

$$\theta(t) = \Theta(t) A \cos(g\mu_B Bt/\hbar) \exp(-t/\tau), \tag{2}$$

where $\Theta(t)$ is a step function and A is the amplitude of the signal at $t = 0$.

In an ensemble measurement, dephasing arises when there is a distribution of precession frequencies ω across the ensemble. For NCQDs in a magnetic field B, this is caused by a distribution $P(g)$ of g factors. Here, P is a normalized probability distribution, so that $P(g)dg$ represents the fraction of QDs with g factor in a range dg about g. By integrating Eq. (2) multiplied by $P(g)dg$ over all g, we can calculate the ensemble-averaged FR signal

$$\langle\theta(t)\rangle = A\Theta(t) \exp(-t/\tau) \int_{-\infty}^{\infty} P(g)dg \cos(\alpha g t), \tag{3}$$

where $\alpha = \mu_B B/\hbar$. If $P(g)$ is symmetric about a central g factor g_0, then

$$\langle\theta(t)\rangle = A\Theta(t) \exp(-t/\tau) \cos(\alpha g_0 t) \hat{P}(\alpha t), \tag{4}$$

where $\hat{P}(\alpha t)$ is Fourier transform of the g-factor distribution with respect to αt and represents the decay envelope caused by inhomogeneous dephasing.

Because of the existence of the S_1 and S_2 components discussed above, we must include different sets of parameters for each relevant component originating from NCQDs in the $X^{\pm}$ states or in the X state, respectively. The expected FR signal is then

$$\langle\theta(t)\rangle = \Theta(t) \sum_{n=1,2} A_n \exp(-t/\tau_n) \cos(g_n \alpha t) \hat{P}_n(\alpha t), \tag{5}$$

where $n = 1,2$ refers to the S_1 and S_2 components.

III. EXPERIMENTAL METHODS AND MATERIALS

We have performed measurements on chemically synthesized CdSe nanocrystal quantum dots purchased from NN-Labs, Inc. These nanocrystals are synthesized by standard techniques with the surface stabilized by octadecyl amine. The NCQDs are suspended at a density of approximately 2 mg/mL in toluene. Here, we present measurements on a sample of NCQDs with mean diameter of 6.1 nm and first absorption peak at 627 nm. The absorption spectrum is shown in Fig. 3(a). The same experiments and data analysis are repeated on NCQDs with mean diameter of 5.7 nm, which lead to similar results. For optical measurements, the NCQD colloidal suspension is placed in a quartz cuvette with optical path length 1 mm. All measurements are at room temperature.

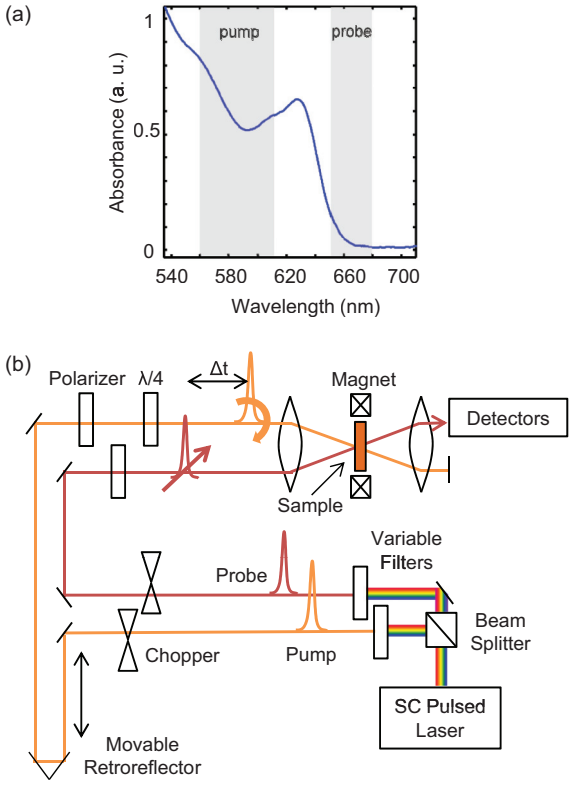

FIG. 3. (Color online) (a) Absorbance spectrum of the CdSe NCQD sample used with $d = 6.1$ nm. The 50-nm-wide pump and 30-nm-wide probe wavelength ranges are shown in gray. (b) Schematic of TRFR experimental setup.

To measure a projection of the spin in the NCQD ensemble, we employ pump/probe Faraday rotation measurements [see Fig. 3(b)]. The pump and probe pulses are derived from a supercontinuum fiber source (Fianium SC450-8PP). This laser provides broad spectrum (white light) pulses with duration ~10 ps, with a repetition rate set to 5 MHz unless otherwise noted. The pump and probe paths are separated by a beam splitter, and each is passed through a linearly graded high-pass and low-pass filter. By adjusting the positions of these filters, we can independently select each beam's center wavelength and bandwidth. The pump and probe wavelength ranges used for measurements are shown in Fig. 3(a). A wide bandwidth for both the pump and probe is used to avoid selectively pumping or probing only a part of the inhomogeneously broadened ensemble of NCQDs. The probe wavelength range is tuned near the lowest energy interband transitions to probe energy-relaxed electrons and holes, whereas the pump wavelength range is tuned to shorter wavelength. The shorter pump wavelength serves to generate electrons and holes in higher energy levels, which avoids effects arising from Pauli blocking, and allows the use of filters to remove scattered pump light from the detectors. The probe and pump are passed through optical choppers at $f_1 = 350$ Hz and $f_2 = 7.5$ kHz,

respectively, to provide modulation for lock-in detection. The pump beam path includes a retroreflector on a motorized delay line which adjusts the delay between the pump and probe arrival at the sample from −0.5 to 16 ns. The pump beam is circularly polarized via a polarizer and quarter waveplate, while the probe is passed through a polarizer to provide linear polarization. The pump and probe are parallel with a separation of about 1 cm and are then passed through the same lens, focusing both beams to the same ∼10-μm-diameter spot within the sample.

The NCQD sample is placed between the poles of an electromagnet which generates a magnetic field perpendicular to the laser propagation direction (the Voigt geometry). The pump pulse generates spin polarized electrons and holes in the NCQDs. The spin state then evolves in time and is measured by the Faraday rotation of the probe pulse. The rotation angle of the probe polarization is then detected using a balanced photodiode bridge and lock-in detection at frequencies f_1 and f_2. By sweeping the pump-probe delay, the dynamics of the ensemble-averaged spin are mapped out in time.

We measure the duration of the pump and probe pulses using a time-correlated photon counting setup (PicoQuant HydraHarp 400) and find pulse half width at half maximum $t_{\text{pump}} \approx 40$ ps for the pump pulse and $t_{\text{probe}} \approx 20$ ps for the probe pulse. The observed FR signal will be spread in time by the finite duration of both pulses effectively performing a convolution of the signal with a pulse with HWHM $t_p \approx \sqrt{t_{\text{pump}}^2 + t_{\text{probe}}^2} \approx 45$ ps. We will see that the signal contains features both with a time scale long compared to t_p and features limited in time by t_p.

Because we are interested in the decay time and envelope of the FR signal, we must check whether the mechanical motion of the delay line introduces position-dependent errors. Specifically, the change in the path length $\Delta x \sim 1.5$ m of the pump beam could give rise to a change in the focus at the sample, due to imperfect collimation or alignment. To measure this effect, we set the pulse repetition frequency to $f_{\text{rep}} = 80$ MHz (repetition period $t_{\text{rep}} = 12.5$ ns). This allows us to observe two pump pulses within the range of the delay line. By comparing the two features separated by t_{rep}, we can determine that these artifacts yield a position dependent error of 2.8% per nanosecond. Over the range of interest of several nanoseconds, this yields an error of ∼10%, which can be considered a systematic error in these measurements.

To measure the inhomogeneity of the NCQD ensemble, we perform TEM measurements and measure size and ellipticity of NCQDs in the resulting images. An aliquot of the NCQD suspension is drawn from the same samples as used for the optical measurements and prepared by drop casting diluted NCQD solution on a TEM grid. A typical image is shown in Fig. 4(a). As discussed above, we consider the NCQDs to be ellipsoidal, with circular cross-section normal to the crystal c axis. In order to measure the ellipticity μ, we must identify NCQDs that are lying with the c axis parallel to the image plane. This can be accomplished with reasonable accuracy by selecting only images where the planes of atoms perpendicular to the c axis are clearly visible in the image, as in the NCQD labeled (A) in Fig. 4(a). [For contrast, the NCQD labeled (B) is not suitably oriented.] The major and minor axes of the NCQD are then measured by placing an ellipse on the image with one axis along the c axis and adjusting the major and minor axes to match the image [see NCQD (C) in Fig. 4(a)]. We have measured the major and minor axes of 182 NCQDs in this sample resulting in the histograms of mean diameter d and ellipticity μ shown in Figs. 4(b) and 4(c). From these measurements of inhomogeneity, we can compare the FR data to models that quantitatively include the effects of ensemble-averaged dephasing and decoherence.

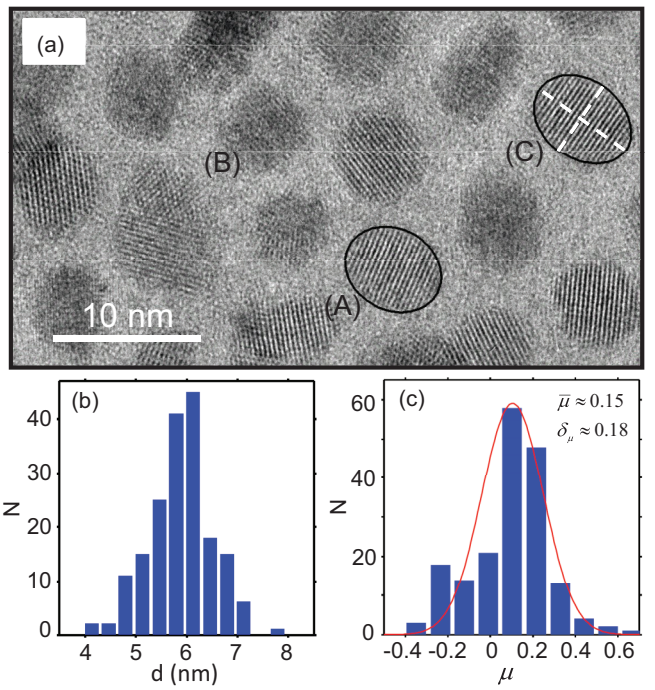

FIG. 4. (Color online) (a) High-resolution TEM image of CdSe NCQDs. (A) and (C) are two example of properly oriented NCQDs used for size and shape measurements. (B) is an NCQD not suitably oriented. Shown in (b) and (c) are size and shape histograms of NCQDs, respectively. The curve in (c) is a *fit to* normal distribution with mean $\bar{\mu}$ and standard deviation δ_μ.

IV. RESULTS

Figure 5(a) shows FR data at $B = 0$ (dashed red) and 200 mT (solid blue). The pump pulse arrival is centered at $t = 0$, where a rapid rise is seen as the spin is initialized. At $B = 0$, the spin signal then decays away over several nanoseconds. At $B = 200$ mT, oscillations are observed in the FR signal as the spin precesses about the applied magnetic field. The Fourier transform (FT) of the $B = 200$ mT data is shown in Fig. 5(b). Two peaks are clearly visible, corresponding to the S_1 and S_2 components. The two-frequency dynamics can also be seen as a slight beating in the time-domain data [see the inset of Fig. 5(a)]. Several features of the data are visible by inspection. The $B = 200$ mT curve has a faster decay envelope than the $B = 0$ curve, indicating B-dependent dephasing or decoherence. The semilog plot of the $B = 0$ data in Fig. 5(c) indicates that the zero-field decay is not exponential, and likely not even biexponential. Below, we will show that the FSD mechanism can explain this $B = 0$ line shape.

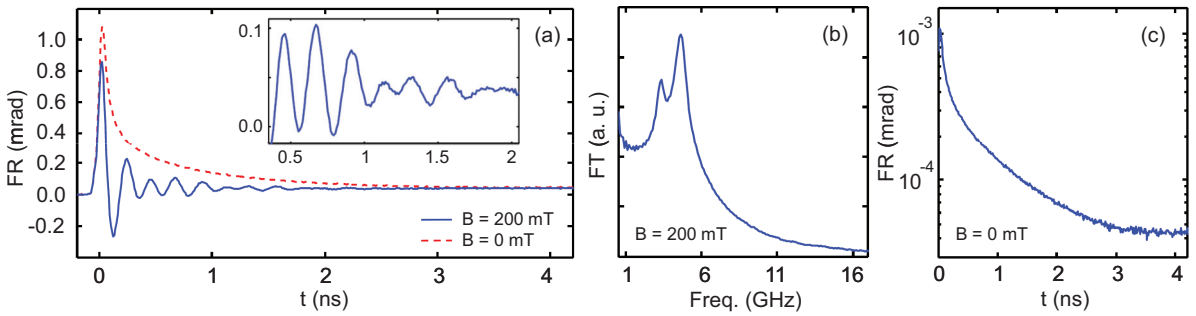

FIG. 5. (Color online) TRFR data: (a) FR vs delay time at $B = 200$ (solid blue) and 0 mT (dashed red). The inset shows a closer view of the data where beating of two oscillation frequencies is evident. (b) FT of the $B = 200$ mT FR data shown in (a). (c) Semilogarithmic plot of FR data at zero magnetic field.

In the next sections, we will compare our experimental results to models including two mechanisms for magnetic-field-dependent spin decoherence and dephasing. First, we will consider the model discussed by Gupta *et al.*,[9] of dephasing arising from inhomogeneous NCQD size (gID) and B-independent decoherence. We will see that the dephasing envelope predicted from the measured NCQD size distribution is in reasonable quantitative agreement with the S_1 component, but not with the S_2 component. Additionally, we find that, as in Refs. 9 and 21, this model does not account for the shorter time-scale features. We then describe the FSD mechanism, arising from rapid transitions between different exciton fine-structure states. In an individual NCQD, this mechanism leads to an exponential decoherence of the spin state. Because the FSS depends sensitively on NCQD size and shape, this results in a distribution of exponential decoherence times, yielding a nonexponential decay of the ensemble spin signal. In addition to the B-dependent effects, we will assume a constant, magnetic-field-independent exponential decay time $\tau_{1,2}$ for the $S_{1,2}$ spin ensembles.

Because the models being used to fit the data here, in general, have a large number of parameters, we must examine cross-correlations between parameters in the model to ensure that the fitting procedure yields meaningful results. The general scheme we will employ is as follows. First, we will manually select realistic initial values β_n for the N_p model parameters and fit a representative data set of FR versus time (t_j,θ_j) with all parameters varied in a nonlinear least squares fit to model function $f(\beta_n;t)$. This will provide a starting value for the $\beta_n = \beta_n^0$ that is at least roughly consistent with the data. Then we obtain the Jacobian matrix $\hat{J}$ with elements

$$J_{jn} = \left.\frac{\partial f(t_j)}{\partial \beta_n}\right|_{\beta_n^0}. \tag{6}$$

The correlation matrix $\hat{C}$ is then obtained with matrix elements

$$C_{jk} = \frac{(\hat{J}^T\hat{J})^{-1}_{jk}}{\sqrt{(\hat{J}^T\hat{J})^{-1}_{jj}(\hat{J}^T\hat{J})^{-1}_{kk}}}. \tag{7}$$

From the $N_p \times N_p$ elements of $\hat{C}$, we can evaluate the degree of independence of each parameter. If $C_{jk} = \pm 1$ for $j \neq k$, then a small change in β_j has the same effect on the model function as a small change in β_k, and these two parameters would be completely correlated. (By definition, $C_{jj} = 1$.) On the other hand, if a small change in β_j alters the model function in a way orthogonal the effect of a small change in β_k, then the two parameters are completely uncorrelated and $C_{jk} = 0$. If two parameters are highly correlated, then those parameters are not well determined by the fit. Below, we will disregard the sign of the cross-correlations and use the matrix $|\hat{C}|$ with elements $|C_{jk}|$. In order to get reliable information from our fitting procedure, we can reparameterize the fit function or hold some parameters constant to reduce cross-correlations, or to isolate cross-correlations in fit parameters that are not of interest.

A. g-factor inhomogeneity induced dephasing

In previous work, inhomogeneous dephasing of spins in NCQDs has been attributed to a normal distribution of g factors arising from nonuniform NCQD size.[9] The size distribution leads to a distribution in quantum confinement, which in turn leads to a distribution of g factors.

The expected dephasing envelope from a g-factor distribution $P(g)$ is given by the Fourier transform $\hat{P}(\mu_B Bt/\hbar)$. From the measured size distribution, we can estimate $P(g)$ using Eq. (1) for the S_1 component and from $g_{\rm exc} = (g_e - 3g_h)/2$ for the S_2 component (again, with the size dependence largely arising from g_e, and g_h taken to be constant). Given this relationship, we expect the widths $\Delta g_{1,2}$ of the g-factor distributions for the $S_{1,2}$ components to be related by $\Delta g_2 = \Delta g_1/2$. The g-factor distributions are then used to estimate the dephasing envelope of S_1 and S_2 components. Figure 6 shows the electron g-factor histogram calculated using the TEM size measurements with fits to both normal (a) and Lorentzian (b) distributions. The shaded region indicates the $1/e$ confidence interval. If $P(g)$ is a normal distribution with standard deviation Δg, the dephasing envelope

$$\hat{P}(t) = \exp\left[-(\Delta g \mu_B t)^2/2\hbar^2\right], \tag{8}$$

which is a Gaussian function with standard deviation $\tau = \hbar/(\Delta g \mu_B)$. If $P(g)$ is a Lorentzian distribution with HWHM Δg, the dephasing envelope

$$\hat{P}(t) = \exp\left(-\Delta g \mu_B t/\hbar\right), \tag{9}$$

which is an exponentially decaying function with time constant $\tau = \hbar/(\Delta g \mu_B)$. As shown in Fig. 6(b), the Lorentzian distribution with $\Delta g_1 = 0.036$ provides a better fit than the normal distribution, as the normal distribution does not capture

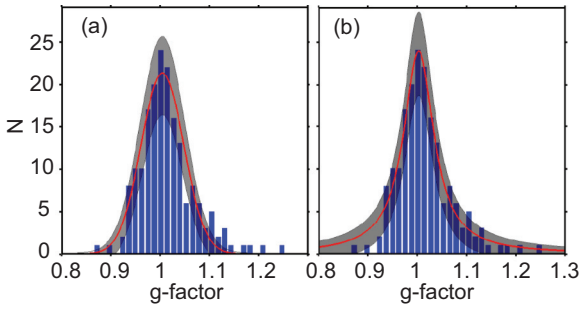

FIG. 6. (Color online) The electron g-factor distribution of NCQDs calculated based on TEM size measurements. The red curves show fits to (a) normal distribution, $\propto \exp[-(g-\bar{g})^2/2\Delta g^2]$, $\bar{g} = 1.005$, $\Delta g = 0.043$ and (b) Lorentzian distribution, $\propto 1/\{1 + [(g-\bar{g})/\Delta g]^2\}$, $\bar{g} = 1.003$, $\Delta g = 0.036$. The shaded regions depict the $1/e$ confidence interval for each bin of data, assuming a Poissonian statistics.

the tails of the histogram in Fig. 6(a). *A priori*, it is unclear what distribution function should be expected for $P(g)$. This distribution is set by the dynamic processes involved in the nucleation and growth of the nanocrystals and likely depends on the specific synthesis protocol.

We can compare the FR data to a model including gID [see Eq. (5)] with different forms of $P(g)$. Additionally, the model must include convolution with the pump and probe pulse temporal profile $f_p(t)$, taken together as a Gaussian function with HWHM t_p. There is a small nonprecessing background $f_{\rm bkg} = a_{\rm bkg}\exp(-t/\tau_{\rm bkg}) + y_{\rm bkg}$, which must be included to achieve a good fit. Such backgrounds have been observed previously,[21,26] and their origin remains unclear. Putting these terms together, we obtain the model function

$$\langle\theta(t)\rangle = [\Theta(t)(A_1 f_1(t) + A_2 f_2(t) + f_{\rm bkg}(t))]\, f_p(t), \qquad (10)$$

where

$$f_n(t) = \cos(g_n \mu_B B t/\hbar)\hat{P}_n(\mu_B B t/\hbar)\exp(-t/\tau_n) \qquad (11)$$

in which $\hat{P}_n$ is either exponential or Gaussian decay envelope for each component, $n = 1,2$, corresponding to a Lorentzian or normal g-factor distribution. The three parameters A_n, Δg_n, and τ_n describe the decay envelope, and g_n describes the coherent dynamics of the S_n component. The main effect of pulse width t_p is a broadening of the step that occurs at $t = 0$. At $t \gg t_p$, the effect of t_p is limited to small changes in the overall amplitude of the signal. We will first focus on exponential $\hat{P}_n$, which is supported by the measured g-factor distribution.

Figure 7(a) shows a fit of the FR data at $B = 200$ mT to Eq. (10) with exponential $\hat{P}_n$, allowing all 12 parameters in the model to vary. Despite the large number of free parameters, the model does not fit the data well. This is because the short-time-scale behavior, $t \lesssim 0.1$ ns, is not characterized by the same lifetime as the longer-time behavior, $t \gtrsim 0.1$ ns. Such a short-time-scale feature is generally observed in FR measurements of NCQDs[9,21,26–29] and is typically ignored either by truncating the data for short times, or by taking the Fourier transform which transfers the short time feature into a broad feature in frequency domain, which can then be ignored. Note that in previous work with shorter pulse duration, this feature appears

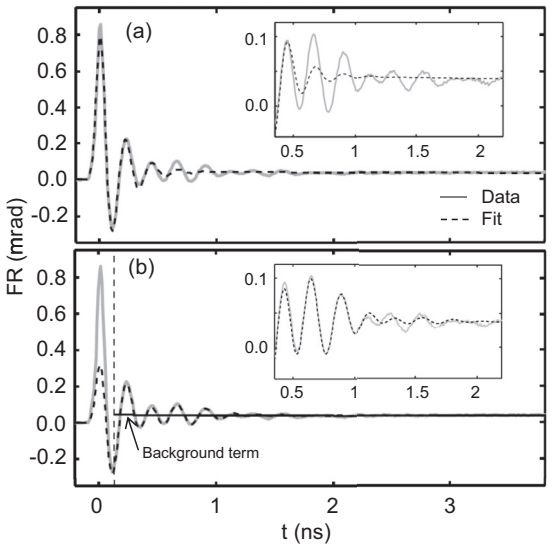

FIG. 7. Fits to gID model at $B = 200$ mT: (a) fit to Eq. (10) with exponential $\hat{P}_n$ (b) Fitting result to the same function with data at $t < 0.13$ ns excluded. The solid black curve in (b) is $f_{\rm bkg}(t)$.

more sharply peaked in time. Therefore it is likely that the width of the short-time-scale feature seen here is set by the pulse width t_p in our experiment. For now, we will follow the strategy of truncating the data, only including $t > 0.13$ ns [indicated by the vertical dashed line in Fig. 7(b)].

Though for now we truncate the short-time-scale data, we do attribute it to FR from optically pumped spins, unlike the case in GaAs where a pulse-width-limited feature is attributed to nonlinear optical effects that do not arise from optical spin pumping.[30] Since these dispersive second-order nonlinear effects do not require excitation, the feature remains prominent at pump energies within the band gap. In this case, we find that the short-time-scale feature disappears at pump energies below the band gap, and in fact scales with pump energy the same as the longer-time-scale FR signal (not shown).

A fit of the FR data at $B = 200$ mT and $t > 0.13$ ns to Eq. (10) with exponential $\hat{P}$ is shown in Fig. 7(b). The inset shows a zoom-in at longer times. Within the time range used for the fit (to the right of the vertical dashed line), the model captures many features of the data well, including the shape of the decay envelope and the coherent precession. Again, it is clear that this model does not capture the short-time-scale behavior.

Given the large number of parameters in the model, it is necessary to study the cross-correlations between model parameters before assigning any credence to the fits. The initially chosen parameters β_n^0 yield an initial set of values for studying the correlations between parameters. Figure 8(a) depicts the correlation matrix $|\hat{C}|$ calculated for the model curve shown in Fig. 7(b) (black = 1, white = 0). The parameters have been grouped to render the matrix roughly block-diagonal. The parameters that are highly correlated with each other can be split into groups. The first two groups correspond to the parameters that govern the shape of the decay envelopes. The S_1 decay envelope is set by A_1, τ_1, and Δg_1, while the S_2 envelope is set mainly by A_2, τ_2, and Δg_2. The pulse width t_p also is correlated with this second group,

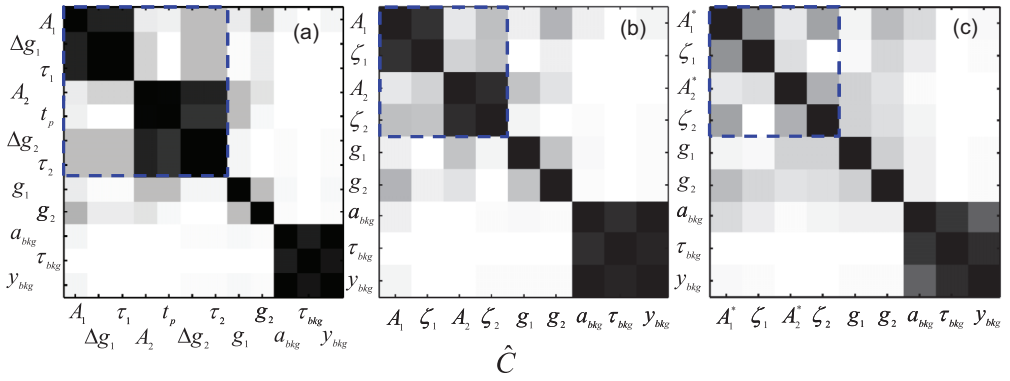

FIG. 8. (Color online) Correlation matrices of fit parameters in gID model. The gray color saturation shows the degree of correlation between the parameters. Black is perfect correlation and white is independence. (a) $|\hat{C}|$ for the initial model [fit shown in Fig. 7(a)] (b) $|\hat{C}|$ when t_p is fixed and the decoherence and correlation times are combined into ζ_n. (c) $|\hat{C}|$ after introducing $A_n^* = A_n \exp(\zeta_n t_0)$.

but with the initial step excluded from the fit, this parameter has very little impact on the model function. The other main group of correlated parameters ($A_{\rm bkg}$, $\tau_{\rm bkg}$, and $y_{\rm bkg}$) govern the small no-precessing background [shown for reference as solid curve in Fig. 7(b)]. Because these background parameters are not of interest for the discussion here, the correlations between them are not of consequence. The remaining two parameters g_1 and g_2 are highly independent of all the other parameters.

The parameters that pertain to the dephasing and decoherence properties, which is the subject of this work, are indicated by the dashed box in Fig. 8(a). Though there exist significant correlations amongst those parameters, they are all quite independent of the parameters outside that group (g_1, g_2, and the three background parameters). In order to deal with the cross-correlations amongst the parameters of interest, first we will note that for both S_1 and S_2 components, we can combine the decoherence and dephasing terms in Eq. (10) into one term $\exp(-t/\tau_n)\hat{P}_n(\mu_B B t/\hbar) = \exp(-\zeta_n t)$, with $\zeta_n = 1/\tau_n + \Delta g_n \mu_B B/\hbar$. Making this change combines the decoherence and dephasing times into a single parameter, but the dephasing and decoherence contributions can be ultimately disentangled by the different B dependence of the two terms in ζ_n. Also, since t_p has little effect on the model function when the initial step is excluded, we will fix $t_p = 45$ ps, at the approximate measured value.

With decoherence and dephasing times combined into the effective decay rates ζ_n and t_p fixed, the resulting correlation matrix is shown in Fig. 8(b). We have reduced the number of parameters needed to capture the behavior of interest from seven to four. There is, however, still fairly significant correlation between a_n and ζ_n. This occurs because $t = 0$ is not included in the fit, where the difference between a change in these two parameters is greatest. We can reduce these correlations with reparameterization $A_n^* = A_n \exp(\zeta_n t_0)$, with a constant $t_0 = 0.23$ ns. This shifts the point where the exponential is equal to unity to $t = t_0$, within the range of the fit. With this change made to both components, the resulting correlation matrix is shown in Fig. 8(c). We now see that only the background terms show significant cross-correlations between themselves, and all of the other parameters are highly independent.

We now perform the least squares fit of eleven datasets ranging from $B = 0$ to 200 mT, to the model described above. These fits have nine free parameters, with four of them pertaining to the behavior of interest. Figure 9 shows three of these data sets and corresponding fits, with the insets showing a zoom of the long-time-scale behavior. Also shown is the correlation matrix for each fit. [The order of parameters in the matrix is the same as in Fig. 8(c)]. All fits show reasonable agreement with the data, and only at the lowest fields do the parameters become significantly correlated. Figures 10(b)–10(e) show the parameters A_n, g_n, and ζ_n versus B, for $B > 40$ mT, where the parameters are largely uncorrelated. The error bars are calculated from QR decomposition of the Jacobian matrix [see Eq. (6)]. We see that the A_n and g_n are

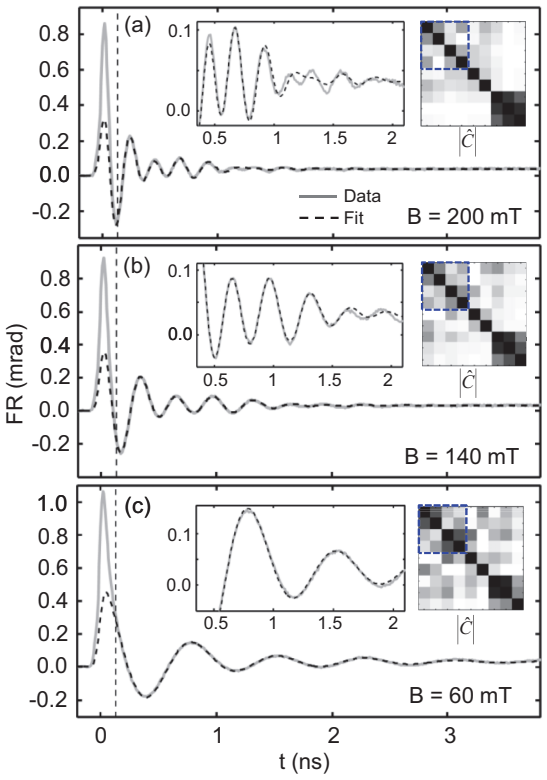

FIG. 9. (Color online) Fits to gID model with reduced parameters. The short-time-scale data($t < 0.13$) are truncated. Insets show a close-up and $|\hat{C}|$. [Matrix elements are ordered as in Fig. 8(c)].

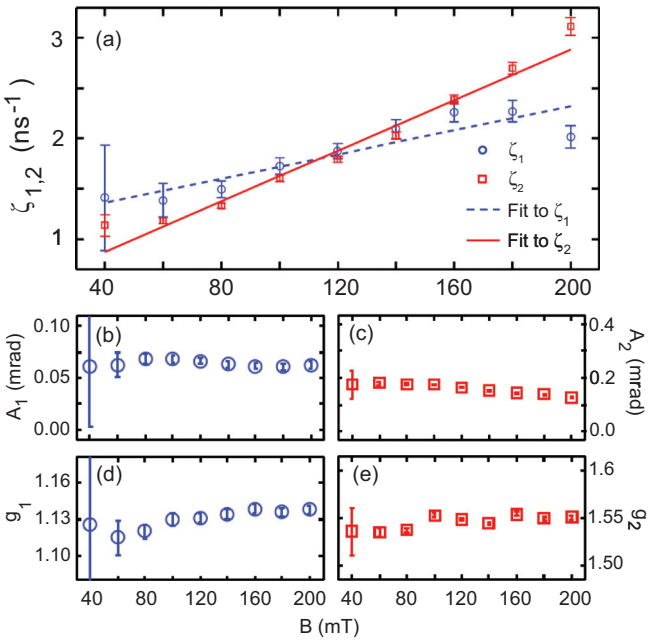

FIG. 10. (Color online) Fit parameters in gID model: (a) $\zeta_{1,2}$ (blue, red) versus B along with linear fits. (b) and (c) show $A_{1,2}$. (d) and (e) depict $g_{1,2}$.

roughly constant. The effective decay rates ζ_n vary linearly, as indicated by the fits shown in Fig. 10(a). From these fits, we can obtain $\tau_1 = 0.89 \pm 0.30$ ns, $\tau_2 = 2.72 \pm 1.79$ ns, $\Delta g_1 = 0.068 \pm 0.03$, and $\Delta g_2 = 0.14 \pm 0.02$.

Though the ζ_n show linear B dependence, in agreement with the model of gID and B-independent decoherence, the values of Δg_n do not agree with the values obtained from the measured size distribution. The values of Δg_1 from the FR data and the size distribution data differ by about a factor of 2, and the corresponding values of Δg_2 differ by about a factor of 8. Moreover, the previously observed size dependence of g_1 and g_2 predicts that $\Delta g_2 \approx \Delta g_1/2$, whereas the fits to the gID model yield Δg_2 significantly larger than Δg_1. This discrepancy may be partly explained by additional sources of g-factor inhomogeneity, such as shape anisotropy and surface structure.[31,32] However, it seems unlikely that these effects would be strong enough to fully explain the discrepancy seen in the S_2 component. This unexpectedly strong dephasing in the S_2 component was also observed in Ref. 9, with no explanation given. In the next section, we find that the FSD mechanism can account for this effect.

The fits to the g-factor distribution as calculated from the size distribution indicate that the dephasing should be better described by an exponential envelope, rather than a Gaussian envelope. Using the values of τ_1 and τ_2 obtained from the fits above (which do not depend on the form of the B-dependent dephasing), we can repeat the fit at $B = 200$ mT using Gaussian $\hat{P}_n$, and compare to the exponential case. The resulting fit is shown in Fig. 11, with $\tau_{1,2}$ fixed, but allowing $\Delta g_{1,2}$ to vary. The exponential case fits the spin signal better than the Gaussian case, as expected, although both fail to capture the short-time-scale peak. This underscores the point that a complete description of the dephasing behavior requires knowledge of the form of the g-factor distribution.

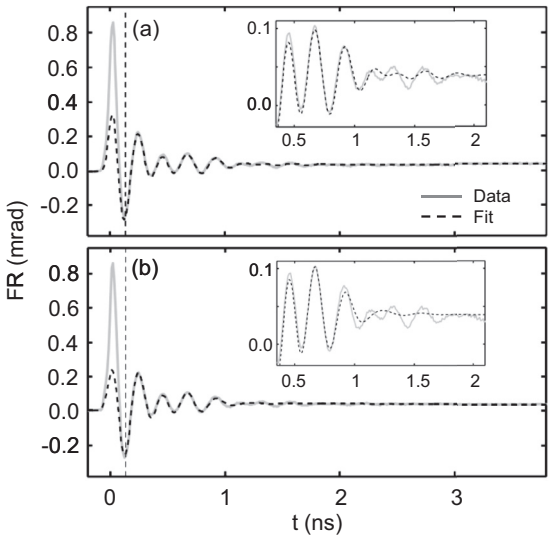

FIG. 11. Fits to gID model with reduced parameters at $B = 200$ mT. The short time data, $t < 0.13$ ns, are not included. (a) and (b) are with exponential and Gaussian $\hat{P}_n$, respectively. Insets show zoom-in at longer times.

The fitting above shows that the FR data can be described by the gID model, though there are weaknesses with this description. First, the short-time-scale behavior must be excluded from the fit. Second, the magnitude of the B-dependent dephasing is larger than expected, especially for the S_2 component. In the next section, we will describe a model that explicitly incorporates the fine structure splitting of the exciton levels and resolves the problems with the gID description.

B. Fine structure-induced decoherence

We now compare the FR data to a model including fine-structure decoherence (FSD) of the spins due to a rapidly fluctuating random splitting arising from transitions between different exciton fine structure states. This model is analogous to the Bir-Aronov-Pikus mechanism for electron spin decoherence caused by bound holes,[33] but with the fluctuating splitting given by a combination of exchange interaction and shape-dependent crystal splitting. Huxter *et al.*[10,20] have measured the rate of transitions between exciton FSS states in NCQDs at room temperature to be $\sim$1 ps^{-1}. At first, this seems in conflict with the approximately nanosecond-scale coherent dynamics seen in the FR measurements. However, FR is sensitive to the net spin of the electrons and holes, regardless of the particular exciton state. For example, a similar effect arises in GaAs, where the electron spin coherence time is much longer than that of the holes.[34] Long-lived spin coherence is observed via FR even though the optically pumped exciton very rapidly loses coherence. The full treatment of optical excitation and quantum evolution in the manifold of exciton fine-structure states is beyond the scope of this work. Here, we will present an effective theory that captures the essential physics, and well describes the data. Furthermore, we will find that the predicted ensemble spin behavior is insensitive to the details of the exciton state dynamics, justifying the simplified model.

The FSD mechanism we describe here is based on two assumptions: (1) the NCQD exciton state is randomly varied on short time scales, but without complete loss of spin information, and (2) there exist NCQDs within the ensemble where the exciton FSS approaches zero in zero applied magnetic field. The first assumption is justified by transient grating measurements[20] that find transition times among exciton states, approximately picosecond, and by TRFR measurements[9] that show coherent spin behavior persisting for time scales of about nanosecond. The second assumption refers to the existence of "quasispherical" NCQDs, as hypothesized by Gupta *et al.*[9] In Fig. 1(c), the calculated FSS displays two crossings at $\mu = \mu_{qs}$. If an exciton state within the ensemble is composed of a linear combination of eigenstates near one of these crossings, then this satisfies the second assumption. To model these two assumptions, we introduce a correlation time τ_c that describes the random variation of the exciton state. As an exciton state varies between superpositions of different eigenstates, the energy splitting fluctuates with a root-mean-squared (rms) magnitude δE given by the magnitude of the FSS in that NCQD. Though δE depends on both NCQD size and shape, we make the simplifying assumption that δE is a function of NCQD ellipticity μ only, and increases linearly away from μ_{qs}. In an applied magnetic field B, the crossing at μ_{qs} becomes an anticrossing with splitting $\Delta \propto B$. Therefore we take

$$\delta E = \sqrt{k^2(\mu - \mu_{qs})^2 + \Delta^2} = \sqrt{k^2(\mu - \mu_{qs})^2 + (\gamma B)^2}, \quad (12)$$

where k and γ are constants that describe the slope of δE versus μ, and the magnitude of δE at the anticrossing, respectively. Figure 12(a) shows $\delta E(\mu)$ at $B = 0$ and at $B \neq 0$ for $k =$ 2 meV, $\gamma = 0.1$ meV, and $\mu_{qs} = 0.41$.

A rapidly fluctuating spin splitting causes decoherence of a spin state with an exponential decay envelope. The decoherence rate $1/\tau$ resulting from an isotropic randomly varying splitting with rms magnitude δE and correlation time τ_c can be calculated in the Born-Markov approximation.[35] In the regime where $\tau_c \ll \tau$,

$$\frac{1}{\tau} = \frac{(\delta E)^2 \tau_c}{\hbar^2}\left[1 + \frac{1}{(g\mu_B B/\hbar)^2 \tau_c^2 + 1}\right]. \quad (13)$$

The results presented here are in the regime where $g\mu_B B/\hbar \ll 1/\tau_c$, so we can simplify

$$\frac{1}{\tau} \approx \frac{(\delta E)^2 \tau_c}{\hbar^2}. \quad (14)$$

Combining Eqs. (12) and (14), we obtain an expression for the decoherence rate

$$\frac{1}{\tau} = \frac{[k^2(\mu - \mu_{qs})^2 + (\gamma B)^2]\tau_c}{\hbar^2}. \quad (15)$$

Figure 12(b) shows the resulting spin decoherence time τ versus μ at $B = 0$ and $B \neq 0$. This mechanism yields greatly varying decoherence times depending on the NCQD shape. At $B = 0$, $\tau(\mu_{qs}) = \infty$, and falls off like $(\mu - \mu_{qs})^{-2}$. At $B \neq 0$, the maximum at μ_{qs} is reduced with $\tau(\mu_{qs}) \propto B^{-2}$ and far from μ_{qs}, also falls off like $(\mu - \mu_{qs})^{-2}$. At large values of $|\mu - \mu_{qs}|$, the calculated decoherence time $\tau < \tau_c$, which is outside the range of validity of Eq. (13). These short time scales, however, are below the resolution of the measurements here, and therefore will not significantly affect the comparison of the model to the data.

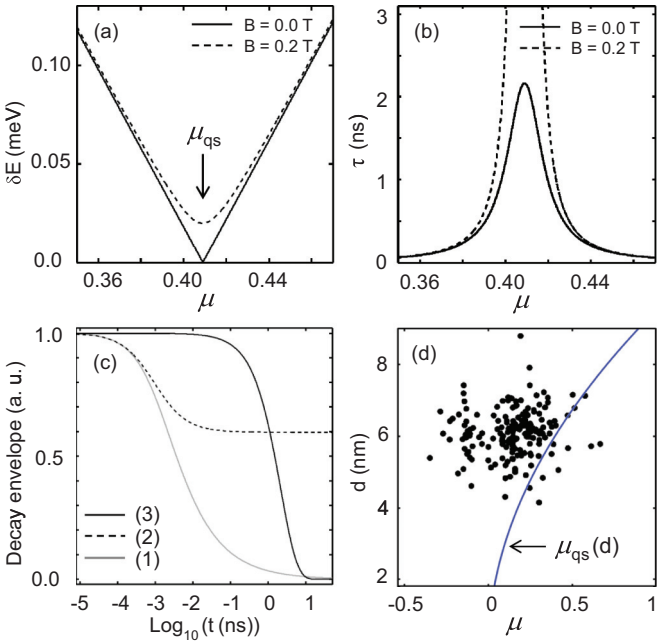

FIG. 12. (Color online) (a) and (b) show δE and τ vs ellipticity μ in the vicinity of μ_{qs} at $B = 0$ T and $B = 0.2$ T. (c) The three terms of Eq. (17). (d) Black circles indicate measured d and μ within the ensemble. The curve shows $\mu_{qs}(d)$. [Curves in (a)–(c) are plotted with $\mu_{qs} = 0.41$, $k = 2$ meV, $\gamma = 0.1$ meV, $\delta_\mu = 0.179$, and $\bar{\mu} = 0.147$.]

The effect of the FSD mechanism in an ensemble measurement must take into account the inhomogeneity of NCQD ellipticity μ, described by a distribution $P(\mu)$. Using the mean ellipticity $\overline{\mu}$ and standard deviation δ_μ found from TEM measurements [see Fig. 4(c)], and assuming a normal distribution, we have

$$P(\mu) = \frac{1}{\sqrt{2\pi}\delta_\mu} \exp\left[\frac{-(\mu - \overline{\mu})^2}{2\delta_\mu^2}\right], \quad (16)$$

as shown in Fig. 4(c). Integrating the exponential decay with lifetime given by Eq. (15) over the distribution $P(\mu)$ we obtain the ensemble decay envelope

$$\Gamma_{FSD}(t) = \frac{1}{\sqrt{1 + 2t\tau_c k^2 \delta_\mu^2/\hbar^2}} \exp\left[\frac{-(\overline{\mu} - \mu_{qs})^2}{\hbar^2/(t\tau_c k^2) + 2\delta_\mu^2}\right] \times \exp(-t\gamma^2 B^2 \tau_c/\hbar^2). \quad (17)$$

The three terms of this equation are plotted in Fig. 12(c), with time on a logarithmic axis. We can see that $\Gamma_{FSD}(t = 0) =$ 1, and then decays to zero as time increases. The first term yields a fast decay at short time scales (~1 ps). The second term modifies the decay at short time scales, but then becomes constant. The main effect of this term is to change the relative amplitude of the short-time-scale behavior and the longer-time-scale behavior. If $\bar{\mu} = \mu_{qs}$ (if the shape distribution is centered at the quasispherical point), then this term is equal to unity. As long as the shape distribution has some amount of

weight at the quasispherical point ($|\overline{\mu} - \mu_{qs}| \lesssim \delta_\mu$), the second term will change the relative amplitude of the fast decay to the slow decay by a factor on the order of unity. Finally, the third term describes an exponential decay with a time constant proportional to $1/B^2$. This term is similar to the dephasing term due to the g-factor distribution but with a decay constant proportional to $1/B^2$ instead of $1/B$.

The exponential decay term in Eq. (17) represents the spin dynamics in NCQDs with $\mu \approx \mu_{qs}$, which is responsible for the nanosecond-scale spin dynamics. The points in Fig. 12(d) show the values of μ and d for all NCQDs measured via TEM. The solid line represents the calculated $\mu_{qs}(d)$. The overlap of $\mu_{qs}(d)$ with the measured scatter of (μ,d) points suggests that we expect NCQDs with long-lived spin coherence to exist within the ensemble. The NCQDs farther from the line in Fig. 12(d) give rise to the observed short-time-scale behavior.

We will now develop a model function, including the gID and FSD mechanisms to explain the magnetic-field-dependent decay envelopes. As discussed above the S_1 component is thought to arise from individual electrons (either in the X^+ state or after recombination of the X^- state),[21] so the splittings due to the hole spin and the electron-hole exchange interaction will not affect the S_1 spin signal, and thus the FSD mechanism will not be active in the S_1 component. Therefore we will model the S_1 component using gID and B-independent decoherence:

$$f_1(t) = \cos(g_1 \alpha t) \exp(-\Delta g_1 \alpha t) \exp(-t/\tau_1). \quad (18)$$

We will model the S_2 component, attributed to NCQDs in the X state, using the same terms as above, with the addition of the FSD ensemble decoherence mechanism:

$$f_2(t) = \cos(g_2 \alpha t) \exp(-\Delta g_2 \alpha t) \Gamma_{FSD}(t) \exp(-t/\tau_2). \quad (19)$$

Γ_{FSD} also depends on parameters $\overline{\mu}$, μ_{qs}, δ_μ, k, τ_c, and γ. We will use the measured values of $\overline{\mu} = 0.147$ and $\delta_\mu = 0.179$ and the calculated value of $\mu_{qs} = 0.409$; the rest of parameters will be discussed below.

As in the previous section, we must closely examine the model and the resulting fits to the data to extract meaningful information, given the large number of parameters. This will be accomplished by studying and reducing the cross-correlations between parameters in the model, where possible. There are a total of 15 parameters in this model for which we choose an initial guess and perform a least squares fit to the data set at $B = 200$ mT, shown in Fig. 13(a).

From Fig. 13(a), we see that this model, unlike the model with gID alone, is capable of describing the data over the entire range, including both long- and short-time-scale dynamics. Figure 13(b) shows the correlation matrix $|\hat{C}|$ for the fit with all parameters varied [see Fig. 13(a)], with the parameters ordered to make $|\hat{C}|$ roughly block-diagonal. Black (white) indicates completely correlated (uncorrelated) parameters. These parameters are grouped according to which parts of the FR signal they affect. The decay envelope of the S_1 component is described by A_1, τ_1, and Δg_1. The short-time-scale portion of the decay envelope of S_2 is described by A_2, k, τ_c, and t_p. The pulse width t_p enters here because the duration of the pump and probe pulses is most prominently seen in the convolution with the very short-time-scale behavior. The longer-time-scale decay envelope S_2 is mainly given by parameters γ, Δg_2, and τ_2, which characterize the random splitting at $\mu = \mu_{qs}$, the

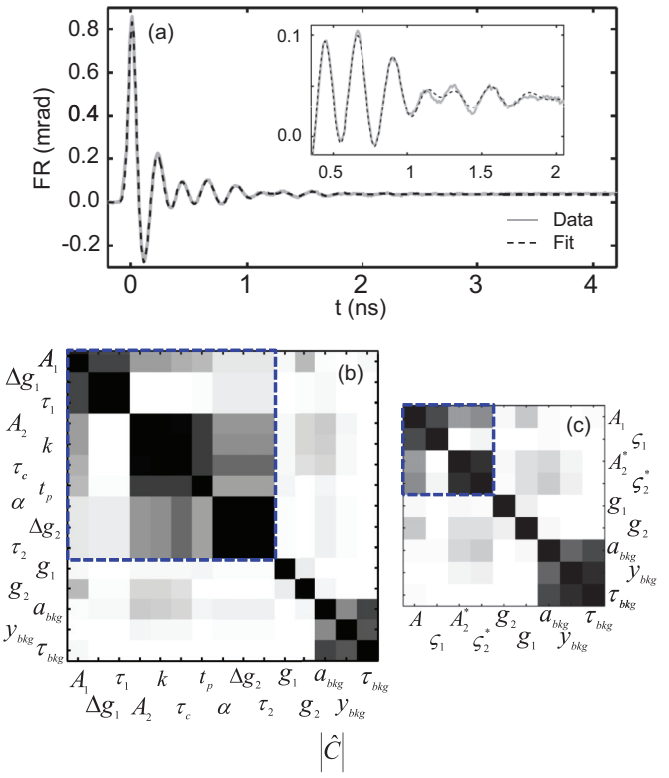

FIG. 13. (Color online) (a) Fit to the gID + FSD model at $B = 200$ mT. The inset shows a close-up. (b) $|\hat{C}|$ for the parameters used in (a). The parameters that primarily define the dephasing and the decoherence dynamics are enclosed in the dashed box. (c) $|\hat{C}|$ with reduced number of parameters by introducing ζ_1 and ζ_2^*. The fit parameter values in (a) are as follows: $\gamma = 0.09$ meV/T, $g_1 = 1.15$, $g_2 = 1.59$, $k = 4.5$ meV, $\tau_1 = 1.5$ ns, $\tau_2 = 1.08$ ns.

gID mechanism, and the B-independent decoherence time, respectively. Again, g_1 and g_2 describe the oscillation of the FR signal, and the final three parameters include a small nonprecessing background.

The parameters we are primarily interested in here are those pertaining to the dephasing and decoherence envelopes, and are highlighted by the dashed box in Fig. 13(b). The remaining parameters describe the spin precession and the background, and are quite un-correlated with the parameters of interest. The high degree of correlation between the parameters that describe the short-time-scale dynamics (A_2, k, τ_c, and t_p) is inevitable given that the details of the dynamics on these short time scales are below the time resolution of the experiment. Therefore we cannot ascribe any significance to the specific values of those parameters. Instead, we will fix three of the four (k, τ_c, and t_p), and only vary A_2 in the fits. The values for these three fixed parameters are all in the expected range: $k = 2.1$ meV matches the typical energy scales of FSS, $\tau_c = 1$ ps agrees with exciton transition rates measured in Ref. 18, and $t_p = 41$ ps is close to the value obtained from time-correlated photon counting. This leaves the correlations within the two sets of three parameters defining the longer-time-scale decay envelopes of the S_1 and S_2 components. As above, we can combine exponentially decaying terms together by using ζ_1 defined above, and $\zeta_2^* = 1/\tau_2 + \Delta g_2 \mu_B B/\hbar + \gamma^2 B^2 \tau_c/\hbar^2$. As before, ζ_1 is a first order polynomial in B, but ζ_2^* is a second order

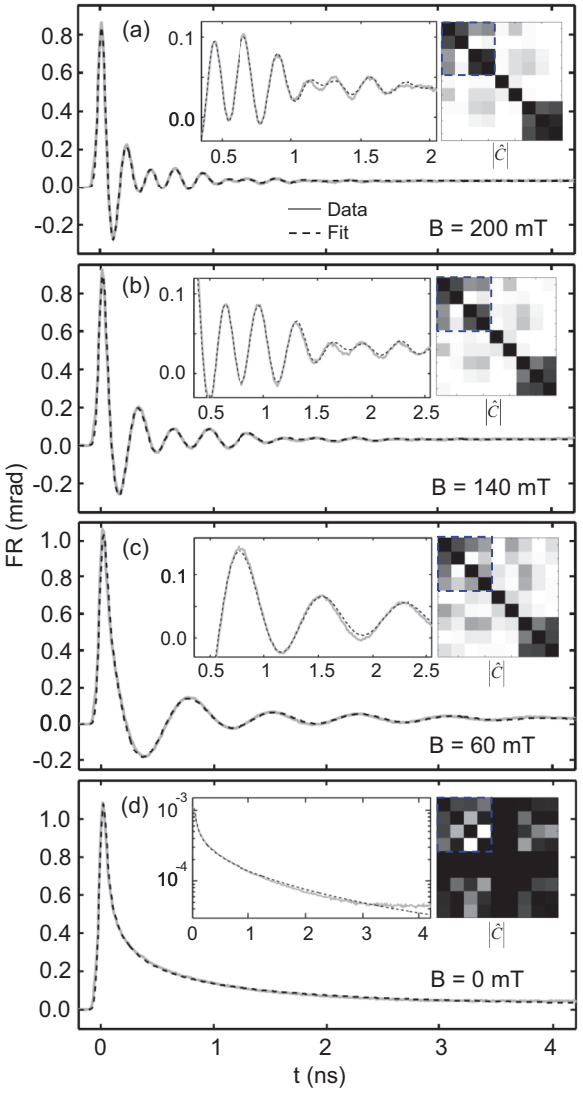

FIG. 14. (Color online) Fits of FR data to gID + FSD model with reduced parameters at different magnetic fields. The insets in (a)–(c) show a close-up of data and the fits along with $|\hat{C}|$. The insets in (d) are semilogarithmic plot of the data and fit along with $|\hat{C}|$.

polynomial in B now that we have added the exponential decay contribution from FSD with decay rate $\propto B^2$. As before, we can further reduce correlations between the decay rates and the amplitudes by shifting the zero of the exponential decay, using the parameter A_2^* defined above. The resulting correlation matrix with reduced parameters is shown in Fig. 13(c).

By making the changes described in the previous paragraph, there are now nine parameters in the model, four of which affect the dephasing and decoherence behavior. The remaining five describe the spin precession dynamics, and a small nonprecessing background. Figure 14 shows the result of fitting the data to this model at several magnetic fields, and the corresponding correlation matrices. From the correlation matrices, we can see that the four dephasing/decoherence parameters are highly uncorrelated from the five other parameters, and the four dephasing/decoherence parameters are only partially correlated amongst themselves at $B \neq 0$. In order to separately extract the different

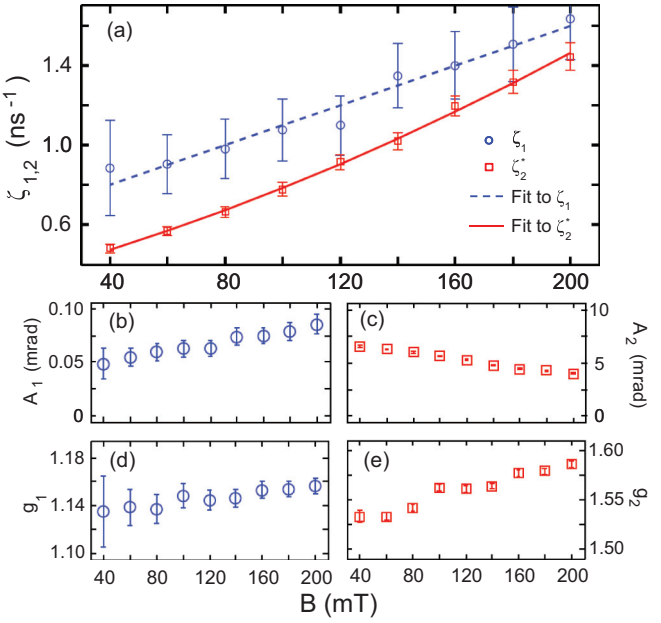

FIG. 15. (Color online) (a) ζ_1 (blue cicles) and ζ_2^* (red squares) vs B along with linear (dashed blue) and second-order polynomial (solid red) fits to them. (b)–(e) show $A_{1,2}$ and $g_{1,2}$ vs B, respectively.

contributions to the decay contained in ζ_1 and ζ_2^*, we fit data sets at 11 magnetic fields from $B = 0$ to 200 mT. The model captures the short- and long-time-scale dynamics at all magnetic fields, well reproducing the shape of the decay envelope. This can be seen further in the semilogarithmic plot of the $B = 0$ data and fit in the inset to Fig. 14(d). The best-fit parameters are plotted in Fig. 15. A_1, A_2, g_1, and g_2 do not vary greatly with B. By fitting ζ_1 versus B to a first-order polynomial and ζ_2^* to a second-order polynomial, we obtain values for τ_1, τ_2, Δg_1, Δg_2, and γ. The fits are shown in Fig. 15(a) with the values obtained listed in Table I.

The value of $\Delta g_1 = 0.057 \pm 0.009$ and $\Delta g_2 = 0.040 \pm 0.011$ are consistent with the values found from the TEM measurements. Significantly, these values agree with the expectation that $\Delta g_2 \approx \Delta g_1/2$. The fact that these values of $\Delta g_{1,2}$ are somewhat greater than those from the TEM size measurements suggests that other sources of g-factor inhomogeneity are present, e.g., surface structure and shape dependence.[31,32] Since γ arises from Zeeman splitting of degenerate states, we expect $\gamma \sim \mu_B \approx 0.0579$ meV/T. The value $\gamma = 0.098$ meV/T agrees with this expectation. Finally, these measurements provide values of $\tau_1 = 1.69 \pm 0.28$ ns and $\tau_2 = 3.11 \pm 0.47$ ns. These decay times are significantly different from each other, and emphasize that the S_1 and S_2

TABLE I. Fit parameters in the gID + FSD model.

Parameter	Value
τ_1	1.69 ± 0.28 ns
τ_2	3.11 ± 0.47 ns
Δg_1	0.057 ± 0.009
Δg_2	0.040 ± 0.011
γ	0.098 ± 0.001 meV/T

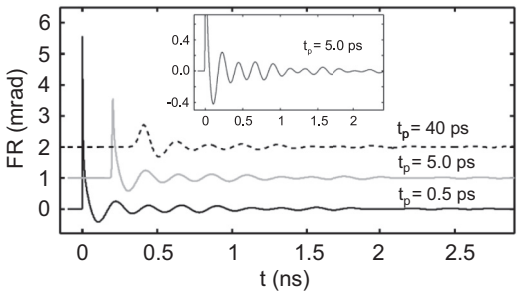

FIG. 16. gID + FSD model function with $t_p = 0.5, 5.0$, and 40 ps. Parameter values are from final fit of the previous section with $B = 200$ mT. Inset shows a close-up of the $t_p = 5.0$ ps curve.

components are subject to different B-independent dephasing/decoherence processes.

V. DISCUSSION AND CONCLUSIONS

Comparison of the FR data to the two models above demonstrates that the gID model is not sufficient to explain the observed behavior, but the addition of the FSD mechanism well-captures the measured decay envelope. To explain the B dependence of the decay envelope using gID alone, the magnitude of the effect for the S_2 component would have to be implausibly large, given both the magnitude of the effect in the S_1 component and the prediction from TEM measurements and effective mass theory. On the other hand, the measured NCQD size and shape distribution are consistent with the gID + FSD model, but not with the gID model alone.

Previous FR measurements in NCQDs have observed the short-time-scale behavior here attributed to FSD.[9,21,26,28] In these works, the short-time-scale behavior is ignored, typically by eliminating the data at short time. These experiments were performed with shorter pump and probe pulse duration, $t_p \sim 100$ fs to $\sim$1 ps. Because in the present work the short-time-scale behavior predicted by FSD is limited by convolution with the pump and probe pulses, the short-time-scale feature has smaller amplitude and larger width than in experiments with shorter pulse duration. Figure 16 shows the gID + FSD model function [see Eq. (10) with $f_{1,2}$ as in Eqs. (18) and (19)] plotted with $t_p = 40$, 5, and 0.5 ps. On the nanosecond scale axes on which the FR data is typically plotted, the short-time-scale feature often appears as a spike with unresolved width. In some previous work, the short-time-scale feature is plotted off the y-axis scale (inset to Fig. 16).

The inclusion of the FSD mechanism in the S_2 component but not the S_1 component is supported by data in Refs. 21 and 26. Both of these results observe spin dynamics in NCQDs that can be tuned to include both the S_1 and S_2 components, or the S_1 component only (by charging the NCQDs electrochemically[21] or by tuning the pump energy).[26] In both cases, the short-time-scale feature is present if and only if the S_2 component is present (see Fig. 2 in Ref. 21 and Fig. 3 in Ref. 26). The FSD mechanism should also be present in the dynamics of lone holes, or in the X^- state with the electrons in a spin zero configuration. We do not observe long-time-scale dynamics reflecting the expected hole g factor, but these states may contribute to the short-time-scale signal.

The procedure used to fit the data here allows for the extraction of the zero-field decoherence times $\tau_1 = 1.69 \pm 0.28$ ns and $\tau_2 = 3.11 \pm 0.47$ ns with reasonable confidence. The fact that these numbers differ with statistical significance suggests that different mechanisms are ultimately limiting the spin coherence time for the S_1 and S_2 components. The S_2 component, associated with carrier spin dynamics in NCQDs containing an exciton, is clearly not limited by the exciton recombination lifetime $\tau_X \approx 20$ ns.[36,37] The lifetime of several nanoseconds is consistent with predictions of decoherence and dephasing caused by randomly oriented nuclear spins,[22,23] which interact with the carrier spins via the hyperfine interaction. We would expect the S_1 component to also be affected by nuclear spin induced decoherence, but as $\tau_1 < \tau_2$, it appears that another mechanism must be further limiting the S_1 lifetime. If the S_1 component arises from the electron spin in the X^+ state, then τ_1 would be limited by the nonradiative recombination of the X^+ state. While the lifetime τ_{X^+} of the X^+ nonradiative recombination is not precisely known, estimates of $\tau_{X^+} \approx 0.7$ ns, are at least of the correct order of magnitude.[38–40] In negatively charged NCQDs, single electron spins can be initialized by a process involving Pauli blocking of transitions to the X^- state.[21] In that process, the electron is polarized in the ground state so there is no possibility of spin decay by recombination. While it is possible that some other mechanism could limit the single electron spin lifetime, the fact that we measure $\tau_1 < \tau_2$ suggests that the S_1 component arises from the electron in the X^+ state, or possibly a combination of X^+ and single electrons polarized via the X^- state.

The results here illustrate that to obtain quantitative information about decoherence and dephasing in NCQDs from a fit to a multiparameter model, there is a need to use a well-defined procedure for fitting the data in which cross-correlations between model parameters are understood. Furthermore, we see that excluding parts of the data in order to improve the quality of the fit, can alter the results, and therefore such fits must be treated with caution.

The FSD mechanism presented here provides a resolution to four separate open questions. First, given the FSS of the exciton ground state in NCQDs, it was unclear how exciton spin dynamics should manifest in this ensemble. This led to the hypothesis that only quasispherical NCQDs give rise to the observed exciton spin precession. This idea is built into the FSD mechanism in that only excitons near the quasispherical point exhibit long-lived spin coherence. Second, FSD correctly reproduces the previously unexplained short-time-scale feature, here caused by exciton spins in NCQDs away from the quasispherical point. Third, FSD accounts for the unexpectedly strong B dependence of the decay of the spin signal for the S_2 component. In this model, this arises from the anticrossing in the FSS near the quasispherical point, which has a splitting proportional to B. Random fluctuations between the levels near this anticrossing cause decoherence at a rate $\propto B^2$. The fitting here reveals this parabolic dependence of the decay rate vs. B. Fourth, transient grating measurements have shown very short lifetimes for excitons in a particular fine-structure state despite long-lived spin coherence observed in Faraday rotation experiments. This has previously been explained by positing that rapid fluctuations do occur between exciton fine structure

states, but without total loss of carrier spin information. In FSD, these rapid fluctuations are the cause of the decoherence of the long-lived carrier spin.

In the discussion of the FSD mechanism here, the exact nature of the fluctuations between different exciton fine-structure states is not discussed. Here, we can avoid this complex issue as the decay envelope predicted by FSD does not depend strongly on these details within the resolution of these measurements, as long as the quasispherical point is included somewhere within the inhomogeneous ensemble, and the random splitting becomes large away from it. This allows us to assume a simple form for the distribution of random splittings, which allows analytical evaluation of the ensemble decay profile. Future work may shed light on how the details of the time evolution of the exciton state within the manifold of fine structure states affects the spin dynamics.

The time-resolved Faraday rotation measurements, combined with TEM characterization of the ensemble and fitting procedures demonstrated here allow for quantitative analysis of decoherence and dephasing effects in NCQDs. Previously, this has proven difficult due to the complexity of the observed dynamics, and the *ad hoc* nature of the model functions used for fitting. These techniques will allow future experiments that study the room-temperature and low-temperature decoherence and dephasing mechanisms in NCQDs in greater detail, with the possibility achieving more robust spin coherence in these semiconductor nanostructures.

ACKNOWLEDGMENTS

The authors are grateful to Reza Sharghi-Moshtaghin for performing TEM imaging. This work was supported by AFOSR, award No. FA9550-12-1-0277.

*Coressponding author: jab298@case.edu

[1]S. A. Wolf, D. D. Awschalom, R. A. Buhrman, J. M. Daughton, S. von Molnr, M. L. Roukes, A. Y. Chtchelkanova, and D. M. Treger, Science **294**, 1488 (2001).

[2]A. Imamoglu, D. D. Awschalom, G. Burkard, D. P. DiVincenzo, D. Loss, M. Sherwin, and A. Small, Phys. Rev. Lett. **83**, 4204 (1999).

[3]D. Loss and D. P. DiVincenzo, Phys. Rev. A **57**, 120 (1998).

[4]O. Gywat, H. J. Krenner, and J. Berezovsky, *Spins in Optically Active Quantum Dots: Concepts and Methods* (Wiley-VCH Verlag GmbH & Co. KGaA, Germany, 2010).

[5]J. A. Gupta, D. D. Awschalom, X. Peng, and A. P. Alivisatos, Phys. Rev. B **59**, R10421 (1999).

[6]D. H. Feng, X. Li, T. Q. Jia, X. Q. Pan, Z. R. Sun, and Z. Z. Xu, Appl. Phys. Lett. **100**, 122406 (2012).

[7]V. Sih, E. Johnston-Halperin, and D. Awschalom, Proc. IEEE **91**, 752 (2003).

[8]I. Žutić, J. Fabian, and S. Das Sarma, Rev. Mod. Phys. **76**, 323 (2004).

[9]J. A. Gupta, D. D. Awschalom, A. L. Efros, and A. V. Rodina, Phys. Rev. B **66**, 125307 (2002).

[10]V. M. Huxter, V. Kovalevskij, and G. D. Scholes, J. Phys. Chem. B **109**, 20060 (2005).

[11]J. M. Luttinger and W. Kohn, Phys. Rev. **97**, 869 (1955).

[12]A. V. Rodina, A. L. Efros, and A. Y. Alekseev, Phys. Rev. B **67**, 155312 (2003).

[13]A. I. Ekimov, F. Hache, M. C. Schanne-Klein, D. Ricard, C. Flytzanis, I. A. Kudryavtsev, T. V. Yazeva, A. V. Rodina, and A. L. Efros, J. Opt. Soc. Am. B **10**, 100 (1993).

[14]A. L. Efros, M. Rosen, M. Kuno, M. Nirmal, D. J. Norris, and M. Bawendi, Phys. Rev. B **54**, 4843 (1996).

[15]A. L. Efros, Phys. Rev. B **46**, 7448 (1992).

[16]U. Woggon, H. Giessen, F. Gindele, O. Wind, B. Fluegel, and N. Peyghambarian, Phys. Rev. B **54**, 17681 (1996).

[17]P. Frantsuzov, M. Kuno, B. Janko, and R. A. Marcus, Nat. Phys. **4**, 519 (2008).

[18]G. D. Scholes, J. Kim, and C. Y. Wong, Phys. Rev. B **73**, 195325 (2006).

[19]C. Y. Wong, J. Kim, P. S. Nair, M. C. Nagy, and G. D. Scholes, J. Phys. Chem. C **113**, 795 (2009).

[20]V. M. Huxter, J. Kim, S. S. Lo, A. Lee, P. S. Nair, and G. D. Scholes, Chem. Phys. Lett. **491**, 187 (2010).

[21]N. P. Stern, M. Poggio, M. H. Bartl, E. L. Hu, G. D. Stucky, and D. D. Awschalom, Phys. Rev. B **72**, 161303 (2005).

[22]J. Schliemann, A. Khaetskii, and D. Loss, J. Phys.: Condens. Matter **15**, 1809 (2003).

[23]I. A. Merkulov, A. L. Efros, and M. Rosen, Phys. Rev. B **65**, 205309 (2002).

[24]S. A. Crooker, D. D. Awschalom, J. J. Baumberg, F. Flack, and N. Samarth, Phys. Rev. B **56**, 7574 (1997).

[25]S. A. Crooker, J. J. Baumberg, F. Flack, N. Samarth, and D. D. Awschalom, Phys. Rev. Lett. **77**, 2814 (1996).

[26]J. Berezovsky, O. Gywat, F. Meier, D. Battaglia, X. Peng, and D. D. Awschalom, Nat. Phys. **2**, 831 (2006).

[27]M. Ouyang and D. D. Awschalom, Science **301**, 1074 (2003).

[28]J. Berezovsky, M. Ouyang, F. Meier, D. D. Awschalom, D. Battaglia, and X. Peng, Phys. Rev. B **71**, 081309 (2005).

[29]Y. Q. Li, D. W. Steuerman, J. Berezovsky, D. S. Seferos, G. C. Bazan, and D. D. Awschalom, Appl. Phys. Lett. **88**, 193126 (2006).

[30]A. V. Kimel, F. Bentivegna, V. N. Gridnev, V. V. Pavlov, R. V. Pisarev, and T. Rasing, Phys. Rev. B **63**, 235201 (2001).

[31]S. J. Prado, C. Trallero-Giner, A. M. Alcalde, V. López-Richard, and G. E. Marques, Phys. Rev. B **69**, 201310 (2004).

[32]J. Schrier and K. B. Whaley, Phys. Rev. B **67**, 235301 (2003).

[33]G. L. Bir, A. G. Aronov, and G. E. Pikus, Zh. Eksp. Teor. Fiz. **69**, 1382 (1975) [Sov. Phys. JETP **42**, 705 (1975)].

[34]J. M. Kikkawa and D. D. Awschalom, Phys. Rev. Lett. **80**, 4313 (1998).

[35]J. Fabian, A. Matos-Abiague, C. Ertler, P. Stano, and I. Žutić, Acta Phys. Slov. **57**, 565 (2007).

[36]B. R. Fisher, H.-J. Eisler, N. E. Stott, and M. G. Bawendi, J. Phys. Chem. B **108**, 143 (2004).

[37]S. A. Crooker, T. Barrick, J. A. Hollingsworth, and V. I. Klimov, Appl. Phys. Lett. **82**, 2793 (2003).

[38]P. P. Jha and P. Guyot-Sionnest, ACS Nano **3**, 1011 (2009).

[39]V. I. Klimov, A. Mikhailovsky, D. W. McBranch, C. A. Leatherdale, and M. G. Bawendi, Science **287**, 1011 (2000).

[40]C. Galland, Y. Ghosh, A. Steinbruck, and V. I. K. M Sykora, and J. A. Hollingsworth, Nature (London) **479**, 203 (2011).